Volume 1
Number 6
December 2025
Pages 889–1186

EES Solar

rsc.li/EESSolar

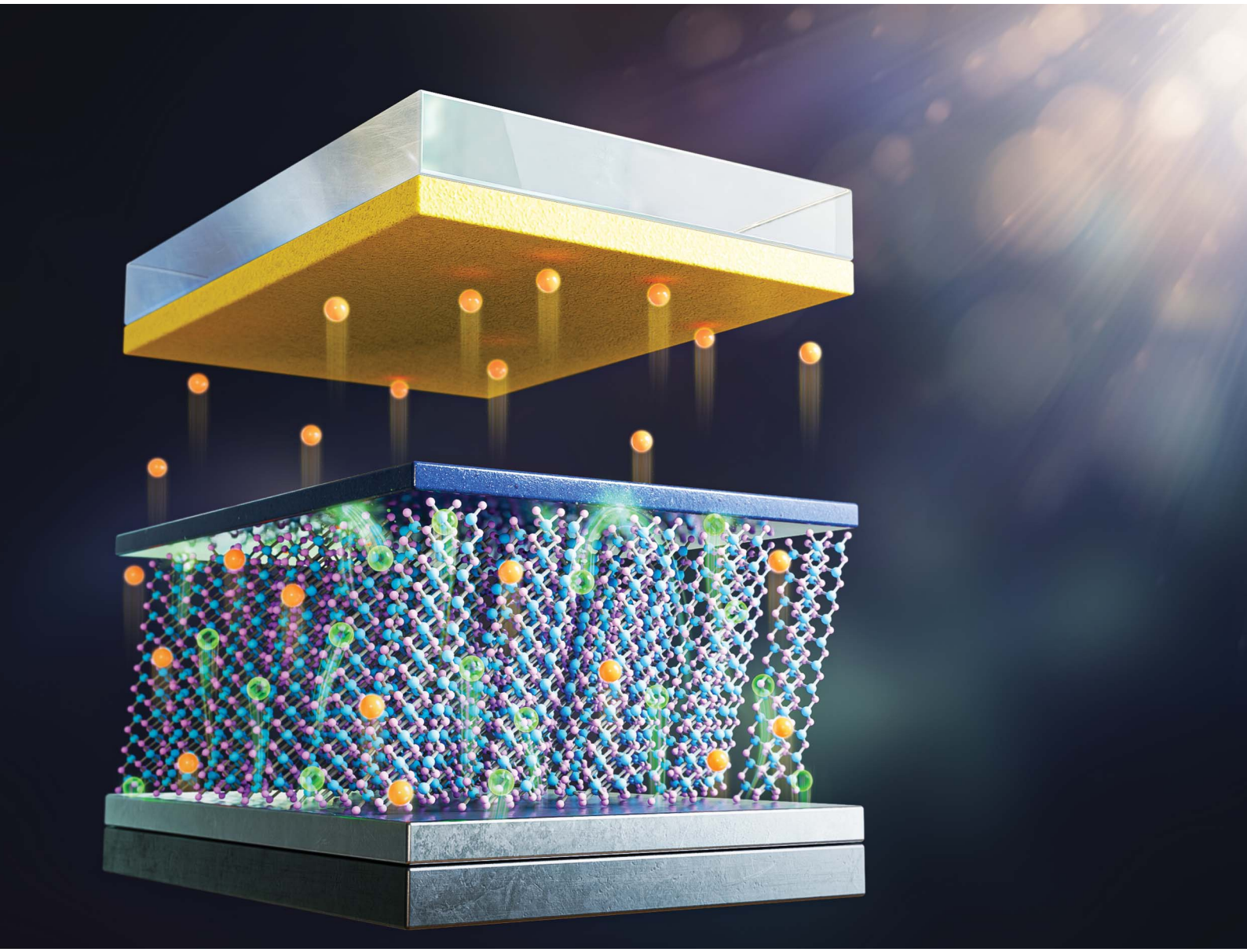

ISSN 3033-4063

ROYAL SOCIETY OF CHEMISTRY

PAPER
William Jo, Shi-Joon Sung, Dae-Hwan Kim *et al.*
Interface engineering of co-evaporated Sb_2Se_3 solar cells using an ALD SnO_x interlayer

EES Solar

PAPER

View Article Online
View Journal | View Issue

Cite this: *EES Sol.*, 2025, **1**, 990

Interface engineering of co-evaporated Sb_2Se_3 solar cells using an ALD SnO_x interlayer

Van-Quy Hoang, †[ab] Jaebaek Lee,†[a] Geumha Lim,[c] Amanat Ali, [d] Bashiru Kadiri-English, [d] Dong-Hwan Jeon, [a] Dae-Ho Son, [a] Hyo Jeong Jo,[a] Dae-Kue Hwang, [a] Kee-Jeong Yang, [a] Eunkyung Cho, [a] Jin-Kyu Kang, [a] William Jo, *[c] Shi-Joon Sung *[ad] and Dae-Hwan Kim *[ad]

Received 13th March 2025
Accepted 3rd September 2025

DOI: 10.1039/d5el00031a

rsc.li/EESSolar

To compensate for the limited efficiency of co-evaporated Sb_2Se_3 solar cells, effective physical and chemical passivation of the interface between the Sb_2Se_3 absorber and the CdS buffer layer was achieved through the deposition of an ultrathin SnO_x interlayer *via* atomic layer deposition (ALD). Due to the passivation effect of the ALD SnO_x interlayer, carrier recombination at both the intra-grain and grain-boundary regions was suppressed, and Sb interdiffusion from the Sb_2Se_3 absorber to the cadmium sulfide (CdS) buffer was effectively blocked. Additionally, the rough surface of the co-evaporated Sb_2Se_3 absorber was mitigated by the conformal deposition of the ALD SnO_x interlayer, reducing the statistical variation in the photovoltaic parameters of the co-evaporated Sb_2Se_3 solar cells. The ultrathin ALD SnO_x interlayer was demonstrated to be a practical strategy for enhancing Sb_2Se_3 solar cell performance regardless of the absorber's morphology, achieving a substrate-type Sb_2Se_3 solar cell with an efficiency of 7.395% through the co-evaporation process.

Broader context

Low-carbon renewable energy technologies are essential to achieving carbon neutrality. Solar energy, an abundant resource, can replace traditional energy sources. While $CuInGaSe_2$ (CIGSe) and kesterite $Cu_2ZnSn(S,Se)_4$ (CZTSSe) are promising thin-film solar materials, their applications are hindered by the use of rare elements and a large open-circuit voltage deficit. Antimony selenide (Sb_2Se_3) has emerged as an alternative due to its 1D crystal structure, high absorption coefficient, and benign grain boundaries. Unlike kesterite, Sb_2Se_3 offers strong anisotropic charge transport, reducing recombination losses. However, challenges such as interfacial recombination, suboptimal band alignment, and interfacial defects limit its efficiency. To enhance Sb_2Se_3 solar cell efficiency, researchers focus on interface passivation, doping engineering, and heterojunction optimization. Deposition techniques like close-space sublimation, hydrothermal deposition, and vapor transport deposition have shown promising results. Advancements in defect passivation and band alignment control are crucial for Sb_2Se_3 to become a commercially viable vacuum thin-film photovoltaic technology, ensuring device uniformity and facilitating large-area fabrication.

1. Introduction

Antimony chalcogenides, such as Sb_2S_3, Sb_2Se_3, and $Sb_2(S,Se)_3$, are well-known compound semiconductors widely used in optoelectronic applications, including photovoltaics, photodetectors, and photoelectrochemical water splitting.[1–3] Due to its unique one-dimensional (1D) crystalline structure, $Sb_2(S,Se)_3$ exhibits excellent potential for high-performance photovoltaics, enabling efficient carrier transport along the 1D framework. Various deposition techniques for forming $Sb_2(S,Se)_3$ absorber layers have been reported, including hydrothermal deposition,[4,5] closed-space sublimation,[6–8] vapor transport deposition,[9,10] thermal evaporation,[11,12] rapid thermal evaporation,[13] injection vapor deposition,[14] sputtering with selenization,[15] and chemical bath deposition (CBD).[16] Although hydrothermal and CBD techniques have achieved Sb_2Se_3 solar cell efficiencies exceeding 10%,[4,16] these solution-based processes pose challenges for large-scale production.

Among various deposition techniques, evaporation has been demonstrated to achieve high efficiency in thin-film solar cells, particularly in $Cu(In,Ga)Se_2$ (CIGS) devices.[17,18] The co-evaporation process offers several advantages, including a tailored multi-step deposition profile for enhanced efficiency, precise control over the crystalline structure of thin films, elimination of the need for an additional crystallization process, and suitability for large-area deposition. However, in Sb_2Se_3 solar cell research, the co-evaporation process has yielded relatively lower efficiencies compared to other

[a]*Division of Energy & Environmental Technology, DGIST, Daegu, 42988, Republic of Korea. E-mail: sjsung@dgist.ac.kr; monolith@dgist.ac.kr*

[b]*Center of Environmental Intelligence, College of Engineering and Computer Science, VinUniversity, Gia Lam District, Hanoi, 14000, Vietnam*

[c]*Department of Physics, Ewha Womans University, Seoul, 03760, Republic of Korea. E-mail: wmjo@ewha.ac.kr*

[d]*Department of Interdisciplinary Engineering, DGIST, Daegu, 42988, Republic of Korea*

† These authors contributed equally to this work.

techniques.[11,12,19–23] Due to the unique 1D crystalline structure of Sb_2Se_3, controlling the morphology of Sb_2Se_3 absorbers remains challenging. Additionally, insufficient selenization during the co-evaporation process can degrade absorber quality and promote defect formation.[24,25]

To enhance the photovoltaic performance of solar cell devices, various passivation techniques are commonly employed during device fabrication.[26–28] In particular, due to the relatively poor quality of co-evaporated Sb_2Se_3 absorber layers, physical and chemical passivation are essential for achieving high-performance Sb_2Se_3 solar cells. Effective passivation of the interface between the Sb_2Se_3 absorber and the CdS buffer layer is critical for improving device efficiency. For solar cell passivation, a metal oxide, TiO_2, is widely used as a passivation layer due to its wide bandgap and specific electrical properties.[6] Additionally, passivation layers play a crucial role in physically smoothing rough absorber layers.[29] The conformal deposition of passivation layers at interfaces enables the formation of a more uniform cross-sectional structure, which is vital for ensuring device uniformity and facilitating large-area fabrication.

In this study, ultrathin SnO_x films deposited *via* atomic layer deposition (ALD) were selected as the interlayer for Sb_2Se_3 solar cells. ALD is a well-established technique for fabricating high-quality, ultrathin films.[30–32] Additionally, due to its conformal deposition capability, ALD enables the formation of uniform thin films on various surfaces, regardless of morphology. These unique characteristics make ALD highly suitable for integrating interlayers into Sb_2Se_3 solar cells. SnO_x is a widely used metal oxide for solar cell passivation due to its wide bandgap, high optical transmittance, superior electron mobility, and chemical stability.[33,34] In this work, the ALD SnO_x interlayer was introduced between the Sb_2Se_3 absorber and the CdS buffer layer, and its role in device performance was systematically investigated.

An ultrathin ALD SnO_x interlayer with a thickness of 2 nm was sufficient to inhibit carrier recombination at the interface between the Sb_2Se_3 absorber and the CdS buffer layer. Due to the reduced carrier recombination, the short-circuit current density (J_{SC}) of Sb_2Se_3 solar cells incorporating the ALD SnO_x interlayer significantly improved. Additionally, the ALD SnO_x interlayer served as an effective barrier to elemental diffusion between the Sb_2Se_3 absorber and CdS buffer layer. Elemental interdiffusion between the absorber and buffer layer is a known factor contributing to the deterioration of the fill factor (FF) in Sb_2Se_3 solar cells.[6,35] In this study, Sb diffusion into the CdS buffer layer was confirmed, and its suppression by the ALD SnO_x interlayer was also observed. Consequently, Sb_2Se_3 solar cells with the ALD SnO_x interlayer exhibited a pronounced enhancement in FF compared to devices without the interlayer.

In addition to its barrier effect, the ALD SnO_x interlayer was found to compensate for the relatively rough surface of co-evaporated Sb_2Se_3 absorbers through uniform and conformal deposition. This morphological passivation effect improved the overall device structure, leading to a narrower distribution of photovoltaic parameters in Sb_2Se_3 solar cells. Furthermore, the impact of the ALD SnO_x interlayer on charge distribution at grain boundaries in Sb_2Se_3 solar cells was observed. The introduction of the ALD SnO_x interlayer weakened band bending at CdS grain boundaries and significantly reduced potential variations. This altered potential profile effectively inhibited carrier recombination at grain boundaries, further enhancing device performance.

The investigation of the ALD SnO_x interlayer in Sb_2Se_3 solar cells demonstrated its effectiveness as a passivation strategy for co-evaporated Sb_2Se_3 solar cells, regardless of absorber morphology. Sb_2Se_3 solar cells incorporating the ALD SnO_x interlayer achieved an efficiency of 7.395%, the highest reported for co-evaporated Sb_2Se_3 solar cells. Further optimization of the ALD SnO_x interlayer has the potential to further enhance device performance.

2. Results and discussion

2.1 Characteristics of thin $MoSe_2$-based devices with a passivation layer

Interfacial engineering at the absorber/buffer interface in Sb_2Se_3-based substrate-configuration solar cells has been extensively studied, particularly with the application of CdZnS or In_2Se to modify energy band alignment and analyze their effects on surface chemistry.[36,37] However, no studies have yet reported the use of an SnO_x layer in substrate-configured cells for absorber surface passivation, though such advancements are expected as the technology continues to develop. In this study, the substrate configuration of Sb_2Se_3 thin-film solar cells was investigated, utilizing the co-evaporation method to enhance efficiency. The source-to-substrate distance was set at 50 cm to ensure a smooth Sb_2Se_3 film and prevent overheating. A detailed schematic of the co-evaporation process is presented in Fig. S1 (SI). The low efficiency of co-evaporated Sb_2Se_3 has primarily been attributed to challenges in fabricating high-quality absorbers in a high-vacuum chamber and the difficulty of controlling pyro-temperatures.

To evaluate the effect of the ALD SnO_x interlayer on device performance, Sb_2Se_3 solar cells were fabricated with a substrate configuration of Mo/$MoSe_2$/Sb_2Se_3/SnO_x/CdS/i-ZnO/AZO/Al. The statistical distributions of power conversion efficiency (PCE), open-circuit voltage (V_{OC}), short-circuit current density (J_{SC}), and fill factor (FF) for devices with and without the ALD SnO_x interlayer are presented in Fig. 1a–d. The results demonstrated that the ALD SnO_x interlayer effectively enhanced the efficiency of Sb_2Se_3 solar cells. Additionally, co-evaporated Sb_2Se_3 solar cells with SnO_x exhibited a narrower distribution of photovoltaic parameters, likely due to the reduced roughness of the Sb_2Se_3/CdS interface facilitated by the ALD SnO_x interlayer. The current density–voltage (J–V) curves of the best-performing devices are shown in Fig. 1e, with the corresponding photovoltaic parameters listed in Table 1. The Sb_2Se_3 solar cell without the ALD SnO_x interlayer achieved a maximum PCE of 3.998%, with a V_{OC} of 0.478 V, a J_{SC} of 22.075 mA cm^{-2}, and an FF of 37.836%. Notably, the Sb_2Se_3 device incorporating the ALD SnO_x interlayer achieved an enhanced PCE of 6.250%, with a V_{OC} of 0.434 V, J_{SC} of 28.007 mA cm^{-2}, and an FF of 51.421%. Among these parameters, J_{SC} and FF exhibited a significant

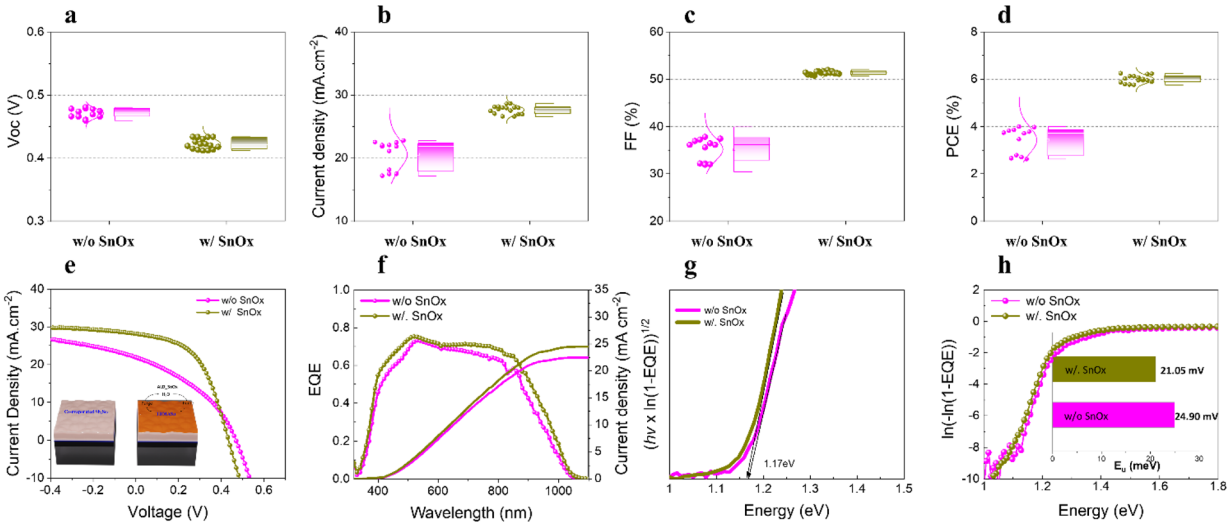

Fig. 1 (a–d) Box plots of solar cell parameters for the tested devices. (e) Current density–voltage (*J–V*) curves of the highest-efficiency device within each group. (f) EQE spectrum of the best-performing device based on the standard AM 1.5G solar spectrum. (g) The bandgap calculated from EQE spectra. (h) Urbach energy values derived from EQE spectra for the control-Sb_2Se_3 and SnO_x–Sb_2Se_3 solar cells, respectively.

increase due to the non-ohmic space-charge-limited current, which contributed to the nonlinear shunt current in Sb_2Se_3 thin-film solar cells. The highly resistive transparent SnO_x layer functioned as a buffer between the CdS window layer, mitigating the formation of shunt paths at the CdS/Sb_2Se_3 interface.[38] This improvement can be attributed to the passivation and protection of the Sb_2Se_3 absorber layer, which reduced recombination losses and enhanced carrier transport within the device. These findings demonstrate the effectiveness of the ALD SnO_x interlayer in improving the efficiency of co-evaporated Sb_2Se_3 solar cells.

The external quantum efficiency (EQE) data in Fig. 1f indicate that both devices exhibited a photoelectronic response from 300 to 1100 nm, with the bandgap of Sb_2Se_3 devices–with and without the ALD SnO_x interlayer. Notably, the two EQE curves displayed identical onset wavelengths, suggesting that both cases of Sb_2Se_3 absorbers had equivalent bandgaps. Previous studies have demonstrated that introducing a high-resistivity SnO_2 layer *via* pulsed laser deposition in the superstrate configuration reduces reflection at the front electrode and enhances carrier collection efficiency.[39] Therefore, the Sb_2Se_3 device with the ALD SnO_x interlayer exhibited increased EQE in the long-wavelength region (600–1100 nm). We observed that the integrated current densities derived from the EQE curves were 22.45 and 24.49 mA cm^{-2} for the control and modified devices, respectively. These values were lower than the J_{SC} measured from the corresponding *J–V* curves. This discrepancy in J_{SC} between the EQE and *J–V* curves has also been reported in previous studies on Sb_2Se_3 solar cells, which can be attributed to the deep levels in the junction region.[16,40] The photogenerated carriers can recombine at these centers at low light levels (EQE measurement), whereas some of these centers are more likely to be occupied due to photoexcitation in high light intensity (under AM 1.5G illumination at 100 mW cm^{-2}).

The indirect bandgaps of devices without and with the SnO_x interlayer were determined to be 1.17 eV, by extrapolating the linear region of the $(h\nu \times \ln(1 - \mathrm{EQE}))^{1/2}$ *versus* $h\nu$ plots to the horizontal photon energy axis (Fig. 1g).[41] The observed bandgap variation was consistent with the chemical composition, as a higher Se content in the co-evaporated Sb_2Se_3 thin film resulted in a lower bandgap value, consistent with our density functional theory (DFT) calculations in the recent discovery.[42] The ALD SnO_x interlayer likely functioned as an efficient electron transport channel between the Sb_2Se_3 absorber and CdS buffer layers, helping electron movement across the Sb_2Se_3/CdS junction. Urbach energy (E_U), a metric used to quantify the

Table 1 Photovoltaic parameters of co-evaporated Sb_2Se_3 solar cells with and without the ALD SnO_x interlayer, measured under AM 1.5G illumination

Samples		V_{OC} (V)	J_{SC} (mA cm^{-2})	FF (%)	PCE (%)	E_g (eV)	E_A (eV)	E_A/E_g (%)	G (mS cm^{-2})	R (Ω cm^2)	A	J_0 (mA cm^{-2})
W/o SnO_x	Average	0.470	20.872	35.468	3.500							
	StDev	0.008	2.157	2.254	0.529							
	Champion	0.478	22.075	37.836	3.998	1.17	1.00	85.47	18.58	0.26	6.10	0.638
w/SnO_x	Average	0.422	27.553	50.911	5.926							
	StDev	0.006	0.657	0.561	0.169							
	Champion	0.434	28.007	51.421	6.250	1.17	1.04	88.89	7.30	2.43	2.08	0.027

extent of the band tail effect, was derived from the ln(1 − EQE)) *versus* energy curve, as shown in Fig. 1h. Upon incorporating the ALD SnO_x interlayer, E_U significantly decreased from 24.90 meV to 21.05 meV, suggesting that recombination near the Sb_2Se_3/CdS junction was mitigated due to the passivation of detrimental defects, a topic further discussed in later sections.

The fabrication techniques for co-evaporated Sb_2Se_3 thin-film solar cells are illustrated in Fig. 2a and described in the "Experimental" section. The surface and cross-sectional morphologies of the as-prepared films were analyzed using scanning electron microscopy (SEM), revealing an estimated Sb_2Se_3 grain size of approximately 290 nm. Fig. 2b–g present top-view SEM images of the co-evaporated Sb_2Se_3 absorbers and CdS buffer layers deposited on Sb_2Se_3, as well as cross-sectional SEM images of the co-evaporated Sb_2Se_3 devices with and without the 2 nm ALD SnO_x interlayer. The SEM images reveal a compact and uniform CdS grain coverage with no visible pinholes between the grains and strong adhesion to the Sb_2Se_3 absorber surface. However, the surface roughness is expected to be high, with wide grain boundaries clear in the surface SEM images. These deep, valley-like grain boundaries could hinder uniform CdS formation. The application of an ALD SnO_x interlayer may mitigate this issue by improving coverage and promoting more uniform CdS growth in these regions. Notably, CdS buffer layer morphology undergoes significant changes with increasing ALD SnO_x interlayer thickness from 0 to 5 nm, as evidenced by the SEM images in Fig. S2, SI. SnO_x is expected to play a crucial role in bridging narrow and deep features that the CdS layer struggles to cover uniformly. However, our findings indicate that CdS exhibits inferior growth on the oxide surface compared to the chalcogenide surface. Increasing the thickness of the ALD SnO_x interlayer altered the morphology of the CdS buffer layers, leading to the formation of discrete nanoparticles. Therefore, to ensure consistent CdS coverage, the SnO_x layer was constrained to an optimal thickness of 2 nm. Furthermore, device performance was highly dependent on the ALD SnO_x interlayer thickness. Notably, only ultrathin ALD SnO_x interlayers enhanced performance, with an optimal thickness of 2 nm, while thicker interlayers (>2 nm) resulted in a decline in V_{OC} (Fig. S3, SI and Table S1).

The crystal structure and phase purity of the co-evaporated Sb_2Se_3 thin film were analyzed using X-ray diffraction (XRD), as shown in Fig. 3a. The Sb_2Se_3 exhibited an orthorhombic crystal structure, classified under the space group Pbnm (JCPDS

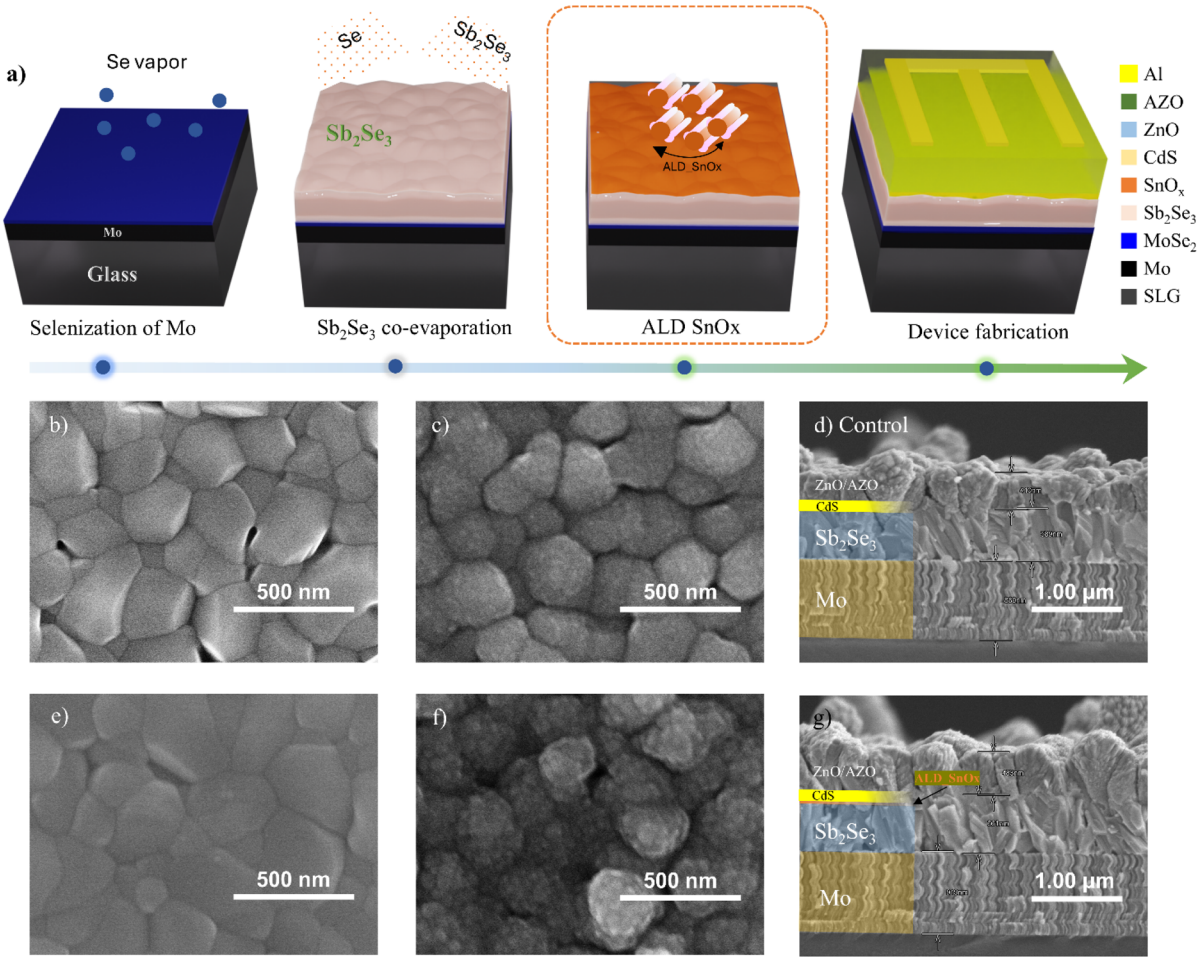

Fig. 2 (a) Schematic representation of the fabrication process for co-evaporated Sb_2Se_3 solar cells with glass/Mo/$MoSe_2$/Sb_2Se_3/SnO_x/CdS/ZnO/AZO/Al architecture. (b–d) Top-view SEM images of the Sb_2Se_3 layer, CdS/Sb_2Se_3 layer, and cross-sectional SEM images of devices without the ALD SnO_x interlayer. (e–g) Corresponding SEM images of devices incorporating the ALD SnO_x interlayer.

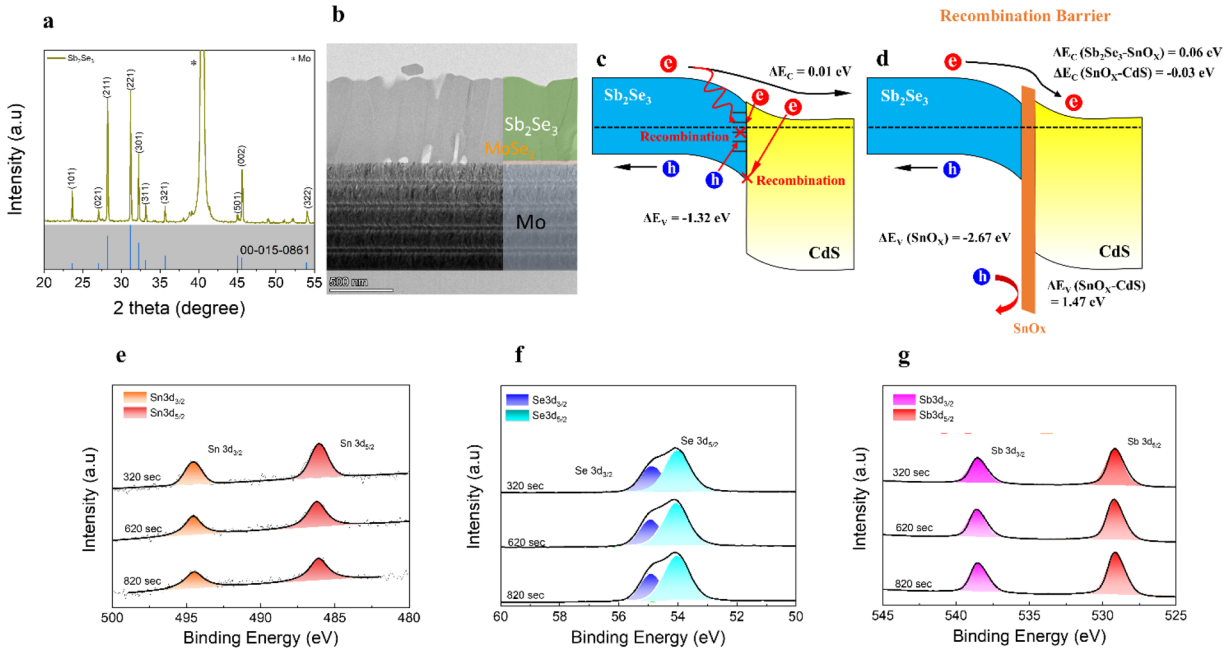

Fig. 3 (a) XRD pattern and (b) HRTEM image of the co-evaporated Sb_2Se_3 absorber on the $MoSe_2$/Mo substrate. (c and d) Energy band structure of the Sb_2Se_3 absorber and CdS buffer without and with the ALD SnO_x interlayer, respectively. (e–g) X-ray photoelectron spectroscopy (XPS) spectra of the co-evaporated Sb_2Se_3 absorber covered with the ALD SnO_x interlayer at various etching depths (320–820 s).

00-015-0861), with no detectable impurity phases. Notably, only strong (*hk1*) diffraction peaks were observed in the XRD pattern, indicating a preferred orientation along the *c*-axis. The intensity ratios I_{101}/I_{221} and I_{002}/I_{221} were 0.13 and 0.34, respectively, confirming the (221)-preferred orientation of the co-evaporated Sb_2Se_3 thin film. To quantify differences in crystalline orientations, the texture coefficient (TC) of the diffraction peaks was calculated using the equation: $\mathrm{TC}_{hkl} = \frac{I_{(hkl)}}{I_{0(hkl)}} \Big/ \left(\frac{1}{N}\sum_{N}\frac{I_{(hkl)}}{I_{0(hkl)}}\right)$, where $I_{(hkl)}$ represents the observed peak intensity of the (*hkl*) plane, $I_{0(hkl)}$ is the corresponding standard XRD intensity, and N is the total number of reflections considered for the calculation.[43] A higher TC value for a given diffraction peak indicates a stronger preferred orientation along that direction. As shown in Fig. S4, SI, the co-evaporated Sb_2Se_3 thin film deposited at 315 °C exhibited a (*hk1*) preferred orientation, particularly along (221) and (211). The cross-sectional high-resolution transmission electron microscopy (HRTEM) image revealed a flat and uniform morphology of the co-evaporated Sb_2Se_3 thin film (Fig. 3b). Additionally, the interplanar *d*-spacing of 0.523 nm corresponded to the (210) planes of orthorhombic Sb_2Se_3, as shown in Fig. S5, SI. This value was consistent with the *d*-spacing observed in one-dimensional (1D) single-crystalline Sb_2Se_3 nanostructures synthesized by other methods.[6,44,45]

The application of an ALD SnO_x interlayer on the Sb_2Se_3 absorber *via* ALD was found to improve J_{SC}, FF, and overall power conversion efficiency. To better understand this improvement, an energy band diagram was constructed based on ultraviolet photoelectron spectroscopy (UPS) analysis, comparing the Sb_2Se_3/CdS and Sb_2Se_3/SnO_x/CdS heterojunctions. The results revealed that the Sb_2Se_3/CdS interface exhibited a weak spike-like conduction band offset (CBO) of $\Delta E_C = 0.01$ eV, whereas the introduction of the ALD SnO_x interlayer led to a more pronounced spike CBO of ΔE_C (Sb_2Se_3–SnO_x) = 0.06 eV in the Sb_2Se_3/SnO/CdS structure. The increased spike CBO effectively suppresses the backflow of electrons, reducing interfacial carrier recombination. In the Sb_2Se_3/CdS heterojunction, the low CBO allowed electrons to transfer easily into CdS; however, it also increased the possibilities of electron backflow and recombination. In contrast, with the SnO_x interlayer, the higher spike CBO restricts electron backflow while maintaining efficient electron transport toward CdS, leading to improved charge transport and increased J_{SC}. However, an excessively large spike CBO can also increase transport resistance, impeding electron injection. This effect can result in charge accumulation, enhanced interfacial recombination, and a reduction in the V_{OC}. As the CBO increases with the insertion of SnO_x, an additional energy barrier is formed at the interface, potentially slowing electron transport. Therefore, in spike-type band alignment, it is crucial to balance electron backflow suppression and forward transport resistance minimization. Experimental results indicate that increasing the SnO_x thickness correlates with a reduction in V_{OC} (Fig. S3, SI). Thus, for optimal device performance, fine-tuning the SnO_x thickness is expected to be an effective strategy for preventing V_{OC} degradation while maintaining J_{SC} improvement. Additionally, the insertion of SnO_x significantly affects the valence band offset (VBO), enhancing the hole-blocking effect. The Sb_2Se_3/SnO_x interface exhibited a substantial increase in VBO to −2.67 eV, effectively preventing hole backflow and reducing hole recombination at the interface (Fig. S6, SI). This strengthened VBO contributes to an increase in J_{SC} and FF, further enhancing

device efficiency. As a result, introducing an ALD SnO_x interlayer improves device performance by forming a spike CBO that effectively blocks electron backflow and enhances J_{SC}. However, an excessive CBO increase can lead to higher transport resistance and a subsequent decrease in V_{OC}. To mitigate this, further optimization of the CBO and precise thickness control of SnO_x are necessary. Furthermore, the increased VBO resulting from SnO_x insertion strengthens hole blocking, reducing recombination and positively impacting J_{SC} and FF. These findings demonstrate that SnO_x incorporation is an effective strategy for improving Sb_2Se_3-based solar cell performance, highlighting the need for further design refinements to achieve optimal efficiency.

The XPS results at various etching depths (Fig. 3e–g) further support the penetration of SnO_x into the Sb_2Se_3 absorber. The presence of Sn within the vacant regions of the Sb_2Se_3 layer, facilitated by the exceptional coverage of ALD SnO_x, indicates that SnO_x effectively passivated the entire Sb_2Se_3 layer, reducing the probability of shunt path formation. Fig. 3e presents the Sn content within the Sb_2Se_3 absorber at etching depths ranging from 320 s to 820 s. As the etching depth increased, the Sn ion content gradually decreased until reaching the Mo substrate, with the total Sb_2Se_3 thickness estimated at approximately 700 nm. Notably, Sn signals remained detectable even after prolonged etching, providing evidence of the deep penetration achieved by the ALD process, consistent with TEM and SEM analyses. Additionally, the presence of various surface nanorods may have contributed to Sn signal detection during depth profiling, further reinforcing the effectiveness of the coverage. The two peaks at 54.6 and 53.7 eV (Fig. 3f) correspond to Se $3d_{3/2}$ and Se $3d_{5/2}$ of Sb_2Se_3, respectively. Similarly, Fig. 3g shows peaks centered at high binding energies of 538.7 and 529.7 eV, attributed to Sb $3d_{3/2}$ and Sb $3d_{5/2}$ of Sb_2Se_3.[20,46,47] Moreover, the XPS spectra of CdS buffers on Sb_2Se_3 and Sb_2Se_3/SnO_x exhibited no significant peak shifts or the appearance of Cd and S after a 10 s etching time (Fig. S7, SI).

The ALD SnO_x interlayer would likely affect charge transport between Sb_2Se_3 and CdS, potentially resulting in an alteration of the electrical potential distribution. The Kelvin probe force microscopy (KPFM) method was employed to investigate potential variations within the CdS layer by measuring surface potential distribution. The topography and local potential mapping results obtained on the CdS surface with and without SnO_x are presented in Fig. 4a. The histogram of contact potential distribution (V_{CPD}) was extracted from the mapping data (Fig. 4b). With the introduction of the ALD SnO_x interlayer, the FWHM of the V_{CPD} distribution decreased from 26 mV to 21.5 mV, showing the formation of a homogeneous potential distribution in the CdS buffer layer. The band bending arising from the irregular potential distribution could exert a force on electrons, the major charge carriers in the CdS layer. Therefore, without the SnO_x layer, localized forces induced near the GBs could generate lateral electron flow, potentially disrupting carrier transport toward the TCO layer.[48] Based on the results, the role of the ALD SnO_x interlayer could be suggested as a capping layer, producing more uniform contact between the absorber and buffer layers by mitigating band bending at GBs.[49] This consequently enables the formation of a more homogeneous and broader p–n junction area, enhancing electron transport across the interface.

To further prove the enhanced charge transport facilitated by the ALD SnO_x interlayer, the band structure of CdS was examined in relation to the presence of SnO_x. We suggest an energy band alignment, as shown in Fig. 4c and Fig. S8, SI, constructed based on ultraviolet-visible (UV-vis) and ultraviolet photoelectron spectroscopy (UPS) measurements. The bandgap of CdS, calculated from UV-vis spectra, was determined to be 2.4 eV for both samples with and without SnO_x. A reduction in the energy difference between E_{CBM} and E_F ($|E_{CBM} - E_F|$) of 50 meV was observed in the CdS with SnO_x compared to CdS without SnO_x. The shift of the Fermi level toward the conduction band minimum (CBM) indicates an increase in electron concentration with the introduction of SnO_x.[50] This confirms improved charge separation at the junction between the Sb_2Se_3 and CdS layers, consistent with the KPFM results. Moreover, a decrease in the work function of 300 meV was observed in CdS with SnO_x. The modified energy band alignment is energetically favorable, inducing a strong built-in potential at the CdS/TCO interface under short-circuit conditions.[51] This configuration can facilitate carrier extraction and contribute to J_{SC} enhancement.[52]

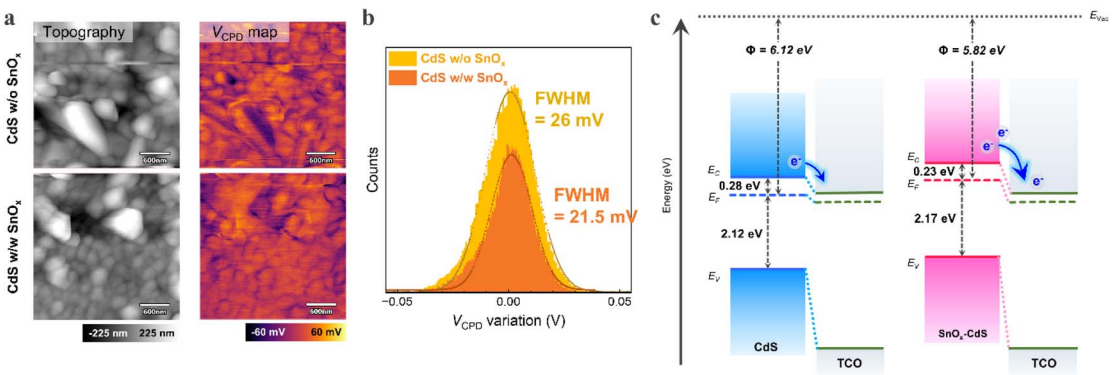

Fig. 4 (a) KPFM images of the CdS buffer layer and (b) histogram of the potential distribution of the CdS surface with or without the ALD SnO_x interlayer and (c) band structure diagram of CdS and SnO_x from UPS measurements.

2.2 Interdiffusion at the absorber–buffer interface

To examine the effect of the ALD SnO_x interlayer on the microstructure of co-evaporated Sb_2Se_3 solar cells, various analytical techniques were employed. High-resolution TEM images of the devices (Fig. S9, SI) provide detailed insights into the microstructural evolution and interfacial characteristics, particularly at the CdS/Sb_2Se_3 and Mo/$MoSe_2$/Sb_2Se_3 interface regions. The introduction of the ALD SnO_x interlayer improved the Sb_2Se_3 device structure, yielding a smoother interface and enhancing the adhesion between the Sb_2Se_3 and CdS layers. For a more precise microstructural analysis, high-angle annular dark-field (HAADF) imaging and energy-dispersive X-ray spectroscopy (EDS) elemental mapping were performed. Fig. S10 and S11, SI present the HAADF images and EDS elemental maps of the Sb_2Se_3/CdS interfacial region, both with and without the ALD SnO_x interlayer. In both cases, Sb and Se elements exhibited uniform distribution throughout the Sb_2Se_3 absorber layer, confirming the homogeneous composition of the material. However, HAADF images of each Sb_2Se_3 device revealed differences in the distribution of layers. The Sb_2Se_3 device with the ALD SnO_x interlayer exhibited improved uniformity of the CdS buffer and AZO transparent conducting oxide (TCO), likely due to morphological changes in the CdS buffer on the ALD SnO_x interlayer. Additionally, EDS elemental composition maps showed no thermally induced interdiffusion, showing that the co-evaporated Sb_2Se_3 absorber and CdS buffer remained free of cross-contamination during the chemical bath deposition (CBD) process of the CdS buffer layer. The EDX line scan further confirmed the absence of thermal diffusion in the heterojunction.

To precisely examine the coverage of the CdS buffer layer on the Sb_2Se_3 absorber and the interdiffusion of elements at the CdS/Sb_2Se_3 interface, HRTEM-EDS analysis was performed. As shown in Fig. 5a–c, spatial elemental mapping of Sb revealed variations in color intensity, indicating notable interfacial interdiffusion of Sb into the CdS buffer layer, whereas no significant interdiffusion of Se was observed (Fig. S12, SI). The presence of Sb in the CdS buffer layer likely resulted from the

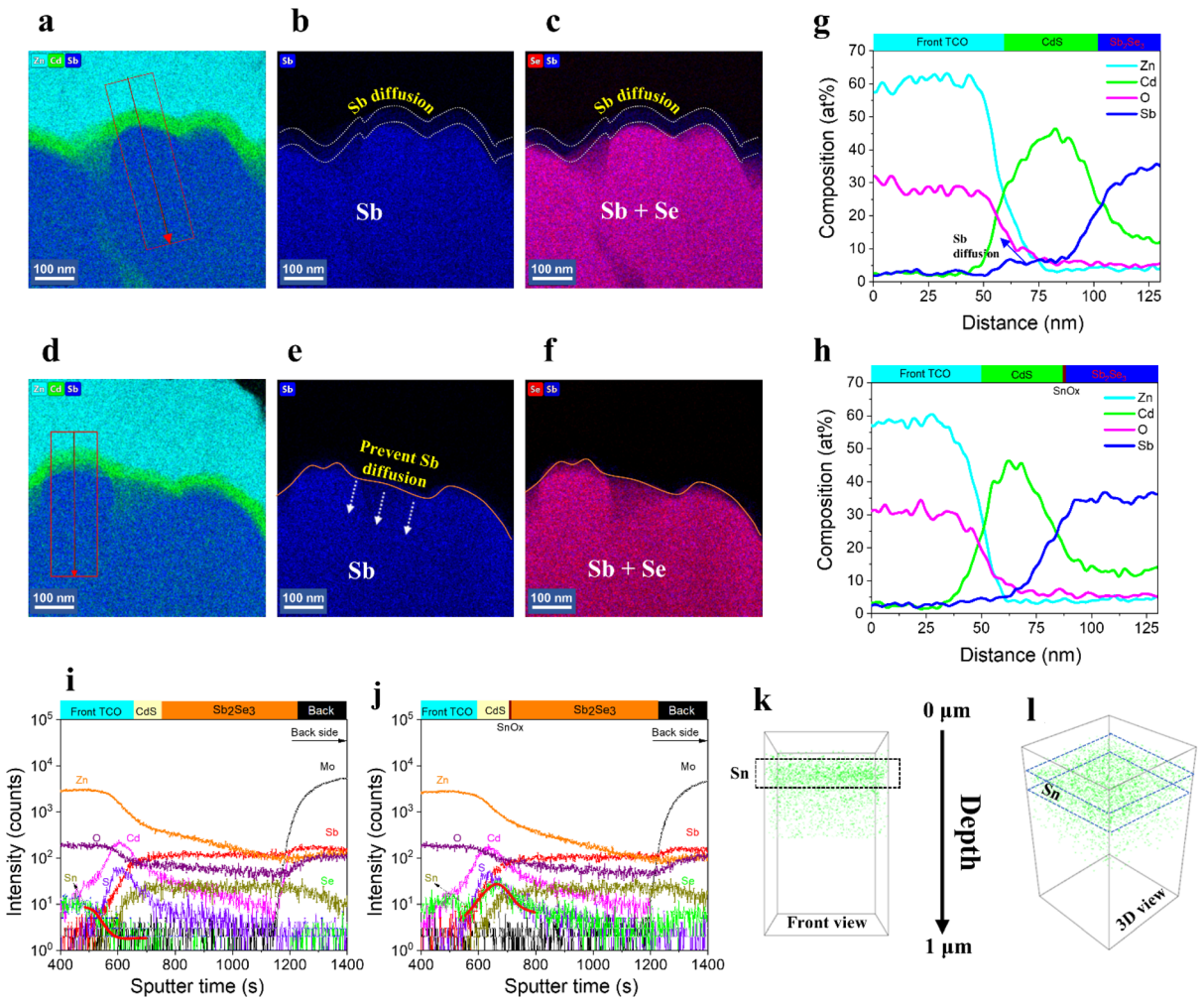

Fig. 5 HRTEM-EDS images of Sb_2Se_3 devices (a–c) without an ALD SnO_x interlayer and (d–f) with an ALD SnO_x interlayer. EDX line scans of Zn, Cd, O and Sb across (g) the TCO/CdS/Sb_2Se_3 interface and (h) the TCO/CdS/SnO_x/Sb_2Se_3 interface. TOF-SIMS depth profile showing elemental mapping of devices (i) without an ALD SnO_x interlayer and (j) with an ALD SnO_x interlayer. TOF-SIMS 3D tomography of the Sn element: (k) front view and (l) 3D view focusing on the Sb_2Se_3/SnO_x interlayer.

dissolution of Sb_2Se_3 in the alkaline ammonia solution, leading to its reaction with NH^{4+} during the CBD process.[6,53–55] However, Sb interdiffusion was mitigated by the ALD SnO_x interlayer, which blocked direct contact between Sb_2Se_3 and NH_4^+ at the Sb_2Se_3/CdS interface (Fig. 5d–f). EDS line scans of Zn, Cd, O, and Sb across the interfaces are presented in Fig. 5g, h. The line scans show a small step increase in Sb over a distance of 30–35 nm in the CdS layer of the control sample, as confirmed by the slight accumulation of Sb at the highest intensity of the Cd signal before a significant increase in the Sb signal. In contrast, no step-function increase was observed for the SnO_x-based device, convincingly suggesting that the SnO_x layer is effective in reducing or preventing the diffusion of Sb into the CdS layer or near the Sb_2Se_3/CdS interlayer.

To verify the presence and interdiffusion of Sb at the Sb_2Se_3 device interface, time-of-flight secondary ion mass spectrometry (TOF-SIMS) depth profiling was performed on Sb_2Se_3 devices with and without the ALD SnO_x interlayer (Fig. 5i and j). In the presence of the ALD SnO_x interlayer, an intense Sn ion signal was detected at the interface between the Sb_2Se_3 absorber and CdS buffer. However, no significant difference in Sb ion concentration was observed due to the low interdiffusion level. These results align with the widespread diffusion pattern identified in the 3D tomography analysis of Sn ions, which were predominantly detected at the Sb_2Se_3/CdS junction along with the absorber thickness (Fig. 5k and l). The TOF-SIMS 3D tomography results for different elements in Sb_2Se_3 devices are shown in Fig. S13, SI. The 3D-rendered overlay of elements further clarifies the position of each component, confirming that Sn ions are incorporated into the Sb_2Se_3 absorber region.

2.3 Carrier transport dynamics and defect characterization

The *J*–*V* curves of the solar cells (Fig. 6a) clearly demonstrate the significant impact of the ALD SnO_x interlayer on the photovoltaic performance of co-evaporated Sb_2Se_3 solar cells. The Sb_2Se_3 device without the SnO_x interlayer exhibited lower power conversion efficiency (PCE), whereas the device with the ALD SnO_x interlayer achieved a higher PCE. The saturation current density and diode ideality factor were extracted using the single–diode equation: $\ln(J + J_{sc} - GV) = \ln(J_0) + \left(\frac{q}{AktT}\right)(V - R_sJ)$, where J_0, G, V, q, A, k, T, and R_s represent the saturation current density, shunt conductance, voltage, electron charge, diode ideality factor, Boltzmann's constant, temperature, and series resistance, respectively.[53] Notably, significant differences were primarily observed in the fill factor (FF) and short-circuit current density (J_{SC}) by analyzing the values of A and J_0 obtained from fitting the $\ln(J + J_{SC} - GV)$ *versus* $(V - RJ)$ curves. Specifically, dV/dJ *versus* $(J + J_{SC})^{-1}$ and dJ/dV *versus* voltage (V) plots (Fig. 6b and c) were used to evaluate the series resistance and average shunt conductance, respectively. Notably, deep defects at grain

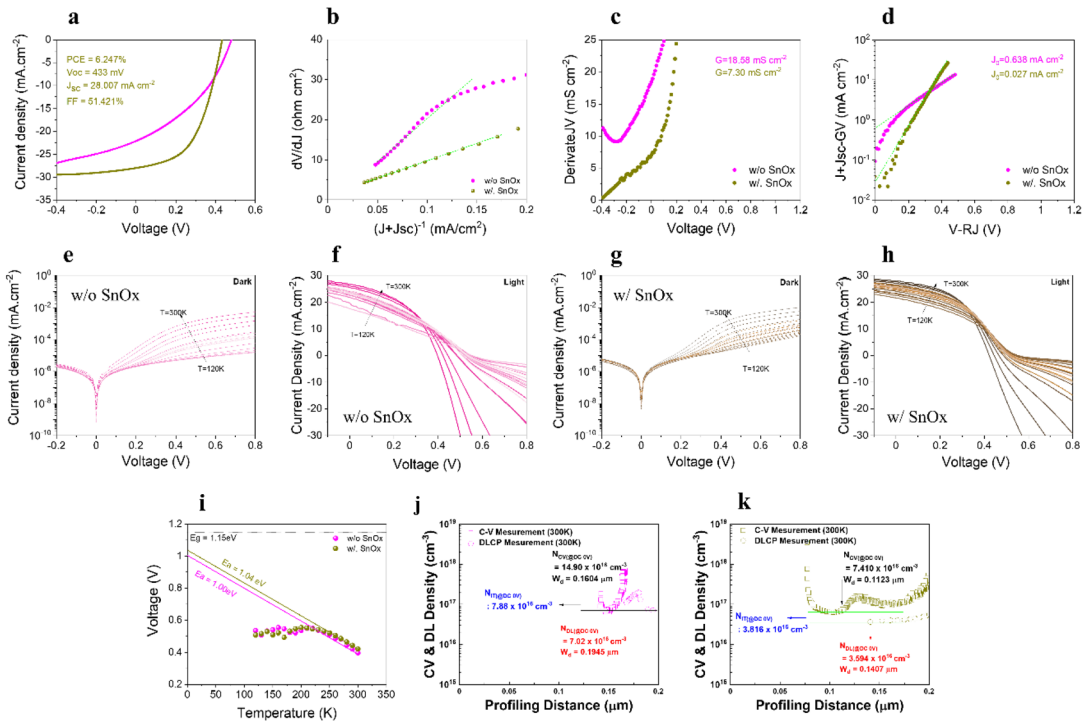

Fig. 6 Characteristic behavior of the best-performing devices: (a) *J*–*V* curves, (b) derivative of dV/dJ under forward bias with fitting used to determine the series resistance and diode ideality factor, (c) derivative of dJ/dV for shunt characteristic analysis, and (d) $\ln(J + J_{SC} - GV)$ *versus* $(V - RJ)$) curves. IVT measurements of Sb_2Se_3 devices under light and dark conditions (120 K to 300 K), showing the determination of series and shunt resistance (e and f) without the ALD SnO_x interlayer and (g and h) with the ALD SnO_x interlayer. (i) Temperature dependence of V_{OC}. Capacitance–voltage (*C*–*V*) and drive-level capacitance profiling (DLCP) of devices (j) without the ALD SnO_x interlayer and (k) with the ALD SnO_x interlayer.

boundaries (GBs) can create alternative paths for electron and hole transport, increasing shunt conductance while maintaining a relatively low series resistance. This phenomenon was observed in the Sb_2Se_3 device without the SnO_x interlayer, resulting in a higher shunt conductance of 18.58 mS cm^{-2}, as shown in Table 1. In contrast, the Sb_2Se_3 device with the ALD SnO_x interlayer exhibited a lower shunt conductance of 7.30 mS cm^{-2} due to defect passivation.[39] As shown in Fig. 6d, the loss mechanisms and variations between the ideal and actual performance of the SnO_x-based devices were analyzed. The values of J_0 and A decreased from 0.638 to 0.027 and from 6.10 to 2.08, respectively, due to reduced recombination at the Sb_2Se_3/CdS interface, attributed to the passivation effect of the ALD SnO_x interlayer. The presence of the ALD SnO_x interlayer resulted in a lower A, indicating reduced recombination losses from interface defects. Additionally, the reduced J_0 in the Sb_2Se_3 device with SnO_x suggests a lower defect density and diminished carrier recombination.

To better understand the impact of the SnO_x interlayer on device performance, we investigated the electrical properties of solar cells over a temperature range of 120 K to 300 K. The electrical characteristics of solar cells are intricately linked with photovoltaic performance and serve as an effective means of examining carrier transport and recombination behavior. Fig. 6e–h presents the temperature-dependent IVT curves under dark and illuminated conditions for devices with and without the ALD SnO_x interlayer. IVT measurements were conducted for all samples at temperatures ranging from 120 K to 300 K. A more pronounced current-blocking effect on injection current was observed at higher temperatures in the Sb_2Se_3 device with the ALD SnO_x interlayer compared to the device without SnO_x.[56] Fig. 6i presents the temperature dependence of V_{OC}, which was analyzed to investigate the recombination characteristics at the Sb_2Se_3/CdS interface. The activation energy (E_A) was figured out by linearly extrapolating the data within the measured V_{OC} temperature range (120 K < T < 300 K), with E_A corresponding to the value at $T = 0$ K. The E_A/E_g ratios were 85.47% for the Sb_2Se_3 device without SnO_x and 88.89% for the device with the ALD SnO_x interlayer. An increase in E_A/E_g correlates with improved photovoltaic performance due to reduced recombination losses from defects at the Sb_2Se_3/CdS interface (Table 1). The recombination mechanism follows the Shockley–Read–Hall (SRH) process in the space-charge region (SCR) when E_A is close to E_g. In contrast, a lower E_A/E_g suggests recombination at the absorber–buffer interface.[57] Therefore, the ALD SnO_x interlayer functioned as a surface passivation layer, mitigating recombination losses at the Sb_2Se_3/CdS interface.[58]

Fig. 6j and k present carrier density as a function of depletion width, obtained from capacitance–voltage (C–V) profiling and drive-level capacitance profiling (DLCP) measurements, to examine the electrical properties near the Sb_2Se_3/CdS interface. The depletion width (W_d) was determined from DLCP measurements by evaluating the capacitance at zero bias and applying the formula $W_d = \varepsilon_0 \varepsilon A/C$, where C is the measured capacitance for each DC bias, A is the device area (0.185 cm^{-2}), and ε is the dielectric constant of the absorber (fixed at 14.3 in this study based on prior assumptions).[41,59] Carrier density N and W_d were extracted from C–V profiling and DLCP measurements. The calculated carrier density (N_{CV}), depletion width (W_d), interface trap density (N_{IT}), and bulk density (N_{DLCP}) are summarized in Table 2. The N_{DLCP} and N_{CV} values for the Sb_2Se_3 device without the ALD SnO_x interlayer were determined to be approximately 7.02×10^{16} cm^{-3} and 14.90×10^{16} cm^{-3}, respectively. With the ALD SnO_x interlayer, these values decreased to approximately 3.59×10^{16} cm^{-3} and 7.41×10^{16} cm^{-3}, respectively. The high density of traps at the interface indicates an increased recombination rate at the Sb_2Se_3/CdS interface, which negatively affects device performance due to significant bulk defects in the Sb_2Se_3 absorber. Both Sb_2Se_3 devices, with and without the ALD SnO_x interlayer, exhibited a relatively wide depletion region. The interface trap density (N_{IT}), defined as the difference between N_{CV} and N_{DLCP} at zero bias, was 7.88×10^{16} for the device without the interlayer and 3.76×10^{16} cm^{-3} for the device with the interlayer. This reduction is consistent with the mitigation of interface recombination observed in IVT measurements. The lower N_{IT} in the ALD SnO_x device confirms the effective passivation of interface traps at the Sb_2Se_3/CdS junction. The interface defect density was reduced by a factor of 2.09 in the SnO_x-treated device, further corroborating that SnO_x effectively suppresses recombination centers, leading to improved device performance.

Table 2 Carrier density parameters of Sb_2Se_3 solar cells with and without the ALD SnO_x interlayer

Samples	N_{CV} (cm^{-3})	W_d (μm)	N_{IT} (cm^{-3})	N_{DLCP} (cm^{-3})
W/o SnO_x	14.90×10^{16}	0.167	7.88×10^{16}	7.02×10^{16}
w/SnO_x	7.41×10^{16}	0.141	3.76×10^{16}	3.59×10^{16}

2.4 Function of SnO_x for the nanorod array Sb_2Se_3/CdS interface

To investigate the coverage of CdS buffer layers on the rough surface of Sb_2Se_3 absorbers and the interdiffusion of elements at the CdS/Sb_2Se_3 interface, we intentionally fabricated nanostructured Sb_2Se_3 absorbers by co-evaporating Sb_2Se_3 onto a 30 nm-thick $MoSe_2$ layer, which is known to promote the formation of an Sb_2Se_3 nanorod array[12] (Fig. S14, SI). As shown in Fig. 7a and b, the introduction of the 30 nm-thick $MoSe_2$ layer facilitated the formation of an Sb_2Se_3 nanorod array on a flat Sb_2Se_3 film. Fig. 7c illustrates the schematic of a nanostructured Sb_2Se_3 solar cell incorporating the thick $MoSe_2$ layer. Unlike the Sb_2Se_3 device with a 5 nm $MoSe_2$ layer, depositing a CdS buffer layer with good coverage on the nanorod array of Sb_2Se_3 on 30 nm $MoSe_2$ was challenging. Incomplete coverage could lead to shunt leakage due to local discontinuities or pinholes at the Sb_2Se_3/CdS junction. Therefore, the nanostructured Sb_2Se_3 absorber required an effective passivation and protection layer to ensure strong adhesion and well-defined junction formation between the Sb_2Se_3 absorber and the CdS buffer layer. Fig. S15, SI presents TEM-EDS images of co-evaporated Sb_2Se_3 solar cells fabricated with thick $MoSe_2$ layers. To address this issue, the ultrathin ALD SnO_x interlayer improved contact between the

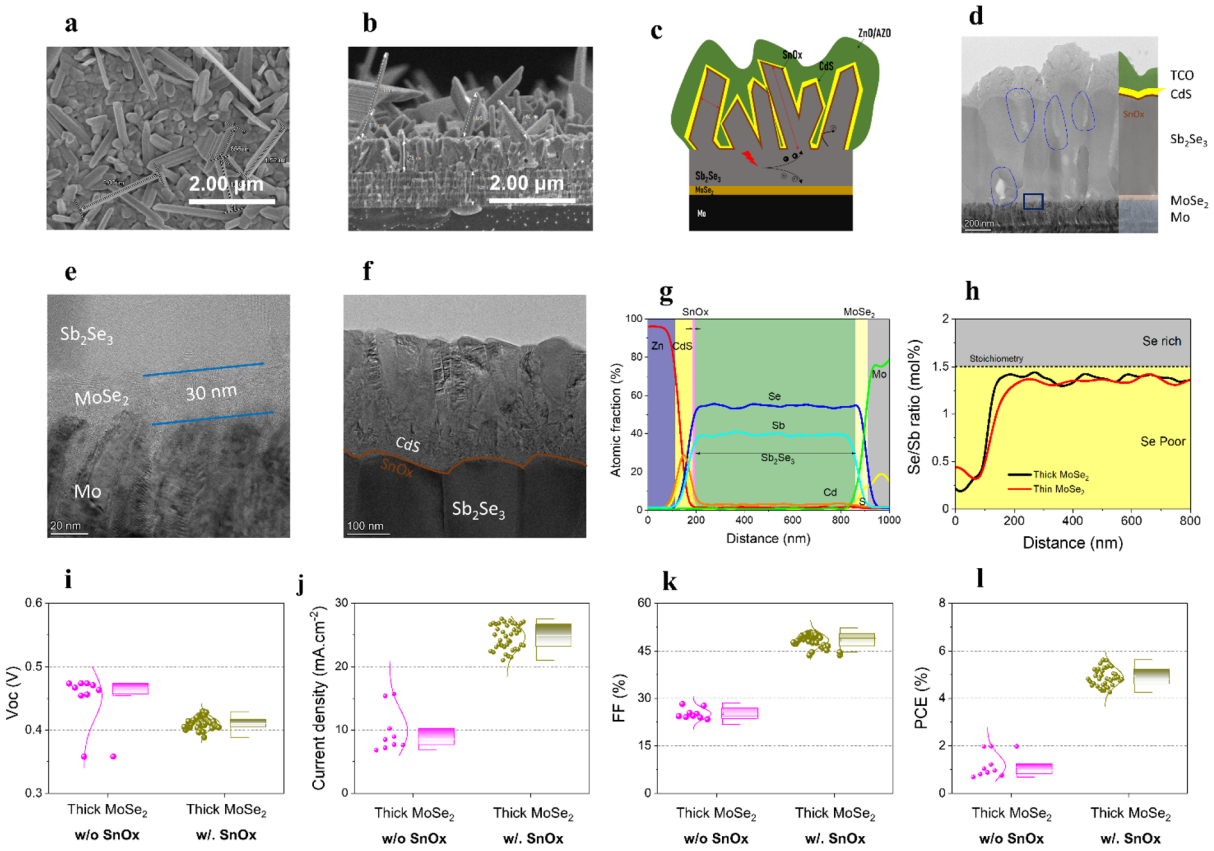

Fig. 7 (a) Top-view and (b) cross-sectional SEM images of co-evaporated Sb_2Se_3 nanorod arrays on a 30 nm-thick $MoSe_2$/Mo substrate. (c) Schematic illustration of the co-evaporated Sb_2Se_3 nanorod array solar cell device. High-resolution cross-sectional TEM (HRTEM) images of (d) the best-performing device, (e) an enlarged HRTEM image of the $MoSe_2$/Sb_2Se_3 interface (highlighted rectangular region), and (f) the Sb_2Se_3/CdS interface. (g) EDX line scans of the device and (h) EDX line scans of the Se/Sb ratio in co-evaporated Sb_2Se_3 devices with varying $MoSe_2$ thicknesses. (i–l) Box plots of the solar cell parameters for co-evaporated Sb_2Se_3 nanorod array devices utilizing the thick $MoSe_2$/Mo substrate.

CdS buffer layer and the rough Sb_2Se_3 nanorod array absorber, thereby reducing shunt leakage and potentially enhancing J_{SC}. The HRTEM images (Fig. 7d and e) clearly showed a 30 nm-thick $MoSe_2$ layer at the interface between Mo and Sb_2Se_3. Further analysis of Sb_2Se_3 films grown on 30 nm-thick $MoSe_2$ revealed that the CdS buffer layer not only covered the top of the absorber but also penetrated the spaces, conformally coating the sidewalls and valleys (Fig. 7f). Although a high density of nanorods was observed in the Sb_2Se_3 absorber grown on thick $MoSe_2$ (as seen in the top SEM image), a region with a flat and compact bottom Sb_2Se_3 absorber was selected for cross-sectional HRTEM analysis to emphasize the role of the $MoSe_2$ layer in facilitating bulk Sb_2Se_3 formation. The location and size of voids within the absorber varied depending on the $MoSe_2$ thickness. As previously observed, small voids formed at the bottom of the absorber in the thin $MoSe_2$-based structure, whereas voids and larger spaces were distributed throughout the absorber in the thick $MoSe_2$-based structure. Thus, the ALD passivation layer played a crucial role in protecting the absorber in deep and inaccessible regions during the CdS deposition process, thereby preventing shunt effects.

Fig. 7g and h presents an EDX line scan of elemental distribution and the Se/Sb ratio (mol%) in Sb_2Se_3 solar cell devices incorporating the ALD SnO_x interlayer with a thick $MoSe_2$ layer. The introduction of a 30 nm-thick $MoSe_2$ layer induced morphological changes in the Sb_2Se_3 absorber while maintaining its chemical composition, as compared to a 5 nm-thick $MoSe_2$ layer. This finding indicates that the optical properties and energy band structure of the Sb_2Se_3 absorber remained unchanged. To assess the charge extraction and passivation effects of the ALD SnO_x interlayer on device performance with a 30 nm-thick $MoSe_2$ layer, Sb_2Se_3 solar cell devices were fabricated with the structure Mo/$MoSe_2$ (30 nm)/Sb_2Se_3/SnO_x/ZnO/AZO/Al electrode. As shown in Fig. 7i–l, the best-performing control device exhibited a PCE of 1.971%, with a V_{OC} of 0.454 V, a J_{SC} of 15.381 mA cm^{-2}, and an FF of 28.200%. In comparison, Sb_2Se_3 devices incorporating the ALD SnO_x interlayer achieved a maximum PCE of 5.627%, with a V_{OC} of 0.414 V, a J_{SC} of 27.214 mA cm^{-2}, and an FF of 49.880% (corresponding values are provided in Table S2). The diode properties of Sb_2Se_3 solar cells based on the thick $MoSe_2$ layer are shown in Fig. S16 (SI), showing an improvement in diode behavior due to the passivation layer. The incorporation of SnO_x at the interface significantly enhanced device performance consistency, even when using inherently rough Sb_2Se_3 films, leading to a narrower distribution of PV parameters.

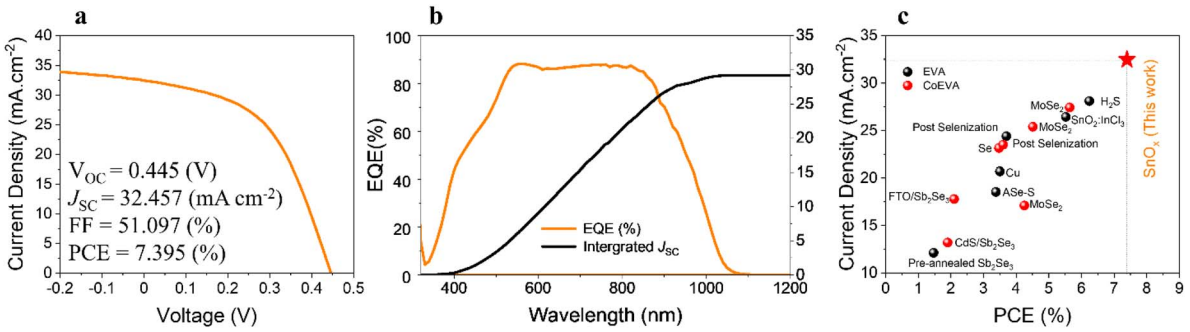

Fig. 8 (a) Current density–voltage (J–V) curve and (b) external quantum efficiency (EQE) spectra of the highest-performing Sb_2Se_3 solar cells fabricated with a passivation layer. (c) Efficiency distribution of Sb_2Se_3 heterojunction solar cells produced using evaporation and co-evaporation methods. An anti-reflective (AR) coating was applied to the device.

Table 3 Detailed photovoltaic performance parameters of high efficiency (co)evaporated Sb_2Se_3 devices

Configuration	PCE (%)	V_{OC} (mV)	J_{SC} (mA cm^{-2})	FF (%)	E_g (eV)	Date	Institute
Substrate	1.47	0.407	12.11	30.00		2018	CNU[60]
Superstrate	1.90	0.300	13.20	48.00		2014	HUST[19]
Superstrate	2.10	0.354	17.80	33.50	1.20	2014	HUST[20]
Substrate	3.38	0.362	18.54	50.39		2023	SRMIST[61]
Superstrate	3.47	0.364	23.14	41.26		2016	HB[22]
Superstrate	3.50	0.339	20.70	49.00		2019	LAPS[62]
Superstrate	3.60	0.352	23.50	44.20		2021	LAPS[23]
Superstrate	3.70	0.335	24.40	46.80	1.18	2014	HUST[63]
Substrate	4.25	0.420	17.11	58.15		2016	HB[21]
Substrate	4.51	0.370	25.39	47.24		2019	DGIST[11]
Superstrate	5.52	0.367	26.44	56.95	1.25	2023	USTC[64]
Substrate	5.63	0.430	27.43	47.35		2021	DGIST[12]
Superstrate	6.24	0.380	28.10	59.10	1.13	2020	CUAS[65]
Substrate	**7.395**	**0.445**	**32.457**	**51.097**	**1.17**	**2024**	**This work**

Additionally, Sb_2Se_3 solar cells with a 30 nm-thick $MoSe_2$ layer showed a reduced variation in photovoltaic parameters, aligning with the previously observed results for Sb_2Se_3 devices using a 5 nm-thick $MoSe_2$ layer.

The Sb_2Se_3 solar cells fabricated on a $MoSe_2$/Mo substrate at 410 °C for 10 minutes were analyzed by an external certified laboratory to confirm our in-house PCE measurements. The J–V and EQE curves of the best-performing devices are shown in Fig. 8, with their photovoltaic parameters summarized in Fig. 8a. The device showed an active area efficiency of 7.395% using an anti-reflective magnesium fluoride (MgF_2) coating, with an FF of 51.097%, J_{SC} of 32.457 mA cm^{-2}, and V_{OC} of 0.445 V. The highest-efficiency Sb_2Se_3 device provided a relatively low J_0 value, showing that the passivation layer effectively reduced photo-generated charge carrier losses (Fig. S17, SI). For further comparison, Fig. 8c and Table 3 summarize the PCEs of this work alongside previously reported Sb_2Se_3 solar cells fabricated using evaporation-based methods. Notably, this study achieved the highest efficiency among (co)evaporation methods using a substrate configuration. The ultra-high vacuum environment used in the (co)evaporation method, often reaching pressures below 10^{-7} torr, ensures superior interface integrity and significantly mitigates defect formation. This results in higher material quality compared to other vacuum-based techniques such as close-spaced sublimation (CSS) or atomic layer deposition (ALD), which typically run at lower vacuum levels (10^{-2} to 10^{-5} torr).

3. Conclusions

We reported an effective passivation method for fabricating high-efficiency Sb_2Se_3 solar cells using the co-evaporation process. An ultrathin SnO_x interlayer, deposited by ALD, was introduced between the Sb_2Se_3 absorber and the CdS buffer layer, resulting in improved J_{SC}, FF, and overall device efficiency. The ALD SnO_x interlayer effectively suppressed carrier recombination at the grain interiors and grain boundaries of the Sb_2Se_3 absorber while serving as a barrier against Sb element interdiffusion. This passivation of the Sb_2Se_3/CdS interface led to a significant enhancement in the performance of Sb_2Se_3 solar cells, regardless of absorber morphology. Additionally, the conformal deposition of the ALD SnO_x interlayer resulted in a uniform device structure, enhancing the reproducibility of co-evaporated Sb_2Se_3 solar cells. As a result, Sb_2Se_3 solar cells with the ALD SnO_x interlayer achieved an efficiency of 7.395%, the highest recorded for co-evaporated Sb_2Se_3 devices. Further optimization of the ALD SnO_x interlayer could lead to performance improvements.

4. Experimental

4.1 Preparation of the ALD SnO_x layer

The SnO_x deposition was conducted using a custom-built ALD system at 100 °C, with TDMASn as the precursor (supported at 45 °C) and O_3 as the oxidizer. The base pressure was kept at 3×10^{-2} torr, with an added Ar flow of 20 sccm under working conditions. During deposition, ALD-SnO_x films on Sb_2Se_3 were heated using a hot trap at 350 °C. The growth rate of SnO_x was determined to be 0.14 nm per cycle, as confirmed by TEM analysis, which measured a 20 nm thickness on a Si wafer after 140 cycles. The average O/Sn ratio was calculated to be 2.781 based on TEM-EDS measurements (Fig. S18, SI).

4.2 Fabrication of the Sb_2Se_3 device

Solar cells were fabricated as a multilayer stack consisting of soda lime glass (SLG)/Mo/Sb_2Se_3/SnO_x/CdS/i-ZnO/ZnO:Al. The Mo back electrode was deposited onto the SLG substrate *via* DC sputtering. A thin $MoSe_2$ layer (~5 nm) was grown at T_{sub} = 600 °C using co-evaporation equipment, while a thicker $MoSe_2$ layer (30 nm) was deposited at T_{sub} = 430 °C for 10 min using a two-zone furnace system. The morphology of the three different Mo substrates is illustrated in Fig. S19 (SI). The Sb_2Se_3 absorber was deposited *via* co-evaporation, using a lower-temperature growth step with T_{source} = 630 °C and T_{sub} = 315 °C. The CdS buffer layer was later deposited *via* chemical bath deposition (CBD) at 65 °C for 11.5 min. The device was completed by sputtering a 50 nm i-ZnO layer followed by a 350 nm ZnO:Al layer (sheet resistance ≈ 30 Ω sq^{-1}). An anti-reflective coating using a magnesium fluoride (MgF_2) anti-reflective film formed by thermal evaporation deposition was only applied to the best cells in this study. Finally, each sample was sectioned into 16 solar cells (active area = 0.185 cm^2) by scribing.

4.3 Characterization

Surface and cross-sectional images were obtained using a field-emission scanning electron microscope (FESEM; Hitachi S-4800). Elemental mapping of the prepared materials was conducted using scanning transmission electron microscopy with energy-dispersive spectrometry (STEM-EDS). Optical absorption spectra were recorded using a UV–visible spectrophotometer (NEOSYS-2000, SINCO Co., Ltd, Seoul, Korea). X-ray diffraction (XRD) analysis was performed using an Empyrean diffractometer (PANalytical Co.) with CuKα radiation (λ = 0.15406 nm) to determine the crystal structure of the films. Raman spectroscopy measurements were conducted using a Raman system equipped with an Mmac 750 spectrometer and a 532 nm excitation laser (irradiation power < 1 mW, spot size 0.7–1 μm). A 532 nm green laser was used, with its power reduced to 1% using an Nd filter. The laser was focused on the sample surface through a 100× magnification lens, and measurements were taken at three locations: left, center, and right of the sample surface. Ultraviolet photoelectron spectroscopy (UPS) spectra were acquired using an ESCALAB 250Xi system (Thermo Scientific Co.) to determine the work function and valence band maximum of the absorber layer surfaces. The elemental distribution of the thin films was analyzed using secondary ion mass spectrometry (SIMS) (TOF-SIMS 5, ION-TOF GmbH). The sputtering source parameters were O^{2+} ions with an energy of 1 keV, a current of 220 nA, an area of 300 × 300 μm, and a sputtered ion dose density (SPIDD) of 3.29×10^{18} ions per cm^2. Amplitude modulation (AM)-mode Kelvin probe force microscopy (KPFM) measurements were performed using a commercial scanning probe microscope (n-Tracer, NanoFocus Inc.) under ambient conditions to investigate local electronic properties. The noncontact mode was used to scan the surface with a Pt/Ir-coated tip (Nanocensors Inc.), maintained at a 50 nm lift height. The scan rate was kept below 0.25 Hz to minimize tip damage. A lock-in amplifier (SR830, Stanford Research Systems Co.) provided KPFM feedback, with an applied AC amplitude of 1.0 V. Current–voltage (*I–V*) curves were recorded under simulated air mass 1.5 global (AM 1.5G) illumination at 100 mW cm^{-2} (1 sun) and 25 °C using a 94022A solar simulator (Newport Co.). External quantum efficiency (EQE) was measured using an SR830 DSP lock-in amplifier system. Temperature-dependent voltage characteristics were analyzed under white light illumination using a source meter (2400, Keithley Co.) with an AM 1.5G spectrum Xe lamp (100 mW cm^{-2}, Abet Technology Co.) over a temperature range of 120–300 K. Capacitance–voltage (*C–V*) and drive-level capacitance profiling (DLCP) measurements were conducted using an LCR meter (E4980A, Agilent) to estimate space charge width and carrier density.

Author contributions

S. J. S. and D. H. K. conceived the idea and directed the overall project. V. Q. H. and J. L. fabricated the devices and conducted the characterization. B. K. E. conducted the CdS CBD process. G. L. and W. J. conducted the KPFM measurements and performed data analysis. A. A. and D. H. S. conducted the *C–V* and DLCP measurements and performed data analysis. D. H. J., H. J. J., D. K. H., J. K. K., E. C. and K. J. Y. participated in discussing the experimental results. V. Q. H. and S. J. S. wrote the manuscript. All authors discussed the results and commented on the paper.

Data availability

The data that support the findings of this study are available from the corresponding author (D.-H. Kim, monolithic@dgist.ac.kr) upon reasonable request.

Supplementary information: Extensive material characterization, including structural and morphological analysis (XRD, TEM, SEM), electronic properties (UPS), and the performance metrics (*J–V* curves, EQE spectra) of the highest-efficiency devices. See DOI: **https://doi.org/10.1039/d5el00031a**.

Conflicts of interest

There are no conflicts to declare.

Acknowledgements

This research was supported by grants from the Korea Institute for Advancement of Technology (KIAT), funded by the Korean government (MOTIE) (No. P0024567), and the National Research Foundation of Korea (NRF), funded by the Korean government (MSIT) (No. RS-2025-02315803, RS-2023-NR076874). This work was also supported by the DGIST R&D programs, funded by the Korean government (MSIT) (No. 25-ET-01, 25-CoE-ET-01). The research at EWU was supported by the Basic Science Research Program through the NRF, funded by the Ministry of Education (No. NRF-2018R1A6A1A03025340) and the Ministry of Science and ICT (No. NRF-2022M3J1A1064229, RS-2024-00355905).

References

1 S. Barthwal, R. Kumar and S. Pathak, *ACS Appl. Energy Mater.*, 2022, **5**, 6545–6585.
2 I. Gharibshahian, A. A. Orouji and S. Sharbati, *Sol. Energy*, 2021, **227**, 606–615.
3 W. Yang and J. Moon, *J. Mater. Chem. A*, 2019, **7**, 20467–20477.
4 Y. Zhao, S. Wang, C. Jiang, C. Li, P. Xiao, R. Tang, J. Gong, G. Chen, T. Chen and J. Li, *Adv. Energy Mater.*, 2022, **12**, 2103015.
5 X. Wang, R. Tang, C. Jiang, W. Lian, H. Ju, G. Jiang, Z. Li, C. Zhu and T. Chen, *Adv. Energy Mater.*, 2020, **10**, 2002341.
6 Z. Li, X. Liang, G. Li, H. Liu, H. Zhang, J. Guo, J. Chen, K. Shen, X. San and W. Yu, *Nat. Commun.*, 2019, **10**, 125.
7 X. Liang, C. Guo, T. Liu, Y. Liu, L. Yang, D. Song, K. Shen, R. E. Schropp, Z. Li and Y. Mai, *Sol. RRL*, 2020, **4**, 2000294.
8 S. Rijal, D. B. Li, R. A. Awni, C. Xiao, S. S. Bista, M. K. Jamarkattel, M. J. Heben, C. S. Jiang, M. Al-Jassim and Z. Song, *Adv. Funct. Mater.*, 2022, **32**, 2110032.
9 G. Liang, M. Chen, M. Ishaq, X. Li, R. Tang, Z. Zheng, Z. Su, P. Fan, X. Zhang and S. Chen, *Adv. Sci.*, 2022, **9**, 2105142.
10 G. Lim, H. K. Park, Y. Wang, S. H. Ji, B. Shin and W. Jo, *J. Phys. Chem. Lett.*, 2024, **15**, 2825–2833.
11 S.-N. Park, S.-Y. Kim, S.-J. Lee, S.-J. Sung, K.-J. Yang, J.-K. Kang and D.-H. Kim, *J. Mater. Chem. A*, 2019, **7**, 25900–25907.
12 S.-N. Park, S.-Y. Kim, S.-J. Lee, S.-J. Sung, K.-J. Yang, J.-K. Kang and D.-H. Kim, *Mater. Adv.*, 2022, **3**, 978–985.
13 K. Li, C. Chen, S. Lu, C. Wang, S. Wang, Y. Lu and J. Tang, *Adv. Mater.*, 2019, **31**, 1903914.
14 Z. Duan, X. Liang, Y. Feng, H. Ma, B. Liang, Y. Wang, S. Luo, S. Wang, R. E. Schropp and Y. Mai, *Adv. Mater.*, 2022, **34**, 2202969.
15 X. Wen, Z. Lu, X. Yang, C. Chen, M. A. Washington, G.-C. Wang, J. Tang, Q. Zhao and T.-M. Lu, *ACS Appl. Mater. Interfaces*, 2023, **15**, 22251–22262.
16 Y. Zhao, S. Wang, C. Li, B. Che, X. Chen, H. Chen, R. Tang, X. Wang, G. Chen and T. Wang, *Energy Environ. Sci.*, 2022, **15**, 5118–5128.
17 V.-Q. Hoang, D.-H. Jeon, S.-Y. Kim, J. Lee, D.-H. Son, K.-J. Yang, J.-K. Kang, S.-J. Sung, D.-K. Hwang and D.-H. Kim, *J. Sci.: Adv. Mater. Devices*, 2024, **9**, 100665.
18 V.-Q. Hoang, D.-H. Jeon, H. K. Park, S.-Y. Kim, W.-H. Kim, D.-K. Hwang, J. Lee, D.-H. Son, K.-J. Yang and J.-K. Kang, *ACS Appl. Energy Mater.*, 2023, **6**, 12180–12189.
19 M. Luo, M. Leng, X. Liu, J. Chen, C. Chen, S. Qin and J. Tang, *Appl. Phys. Lett.*, 2014, **104**, 173904.
20 X. Liu, J. Chen, M. Luo, M. Leng, Z. Xia, Y. Zhou, S. Qin, D.-J. Xue, L. Lv and H. Huang, *ACS Appl. Mater. Interfaces*, 2014, **6**, 10687–10695.
21 Z. Li, X. Chen, H. Zhu, J. Chen, Y. Guo, C. Zhang, W. Zhang, X. Niu and Y. Mai, *Sol. Energy Mater. Sol. Cells*, 2017, **161**, 190–196.
22 Z. Li, H. Zhu, Y. Guo, X. Niu, X. Chen, C. Zhang, W. Zhang, X. Liang, D. Zhou and J. Chen, *Appl. Phys. Express*, 2016, **9**, 052302.
23 V. Kumar, E. Artegiani, P. Punathil, M. Bertoncello, M. Meneghini, F. Piccinelli and A. Romeo, *ACS Appl. Energy Mater.*, 2021, **4**, 12479–12486.
24 C. Chen and J. Tang, *ACS Energy Lett.*, 2020, **5**, 2294–2304.
25 J. Dong, Y. Liu, Z. Wang and Y. Zhang, *Nano Sel.*, 2021, **2**, 1818–1848.
26 Y. Zhang, T. Shi, L. Duan, B. Hoex and Z. Tang, *Nano Energy*, 2024, **131**, 110282.
27 J. Schmidt, R. Peibst and R. Brendel, *Sol. Energy Mater. Sol. Cells*, 2018, **187**, 39–54.
28 P. M. Salomé, B. Vermang, R. Ribeiro-Andrade, J. P. Teixeira, J. M. Cunha, M. J. Mendes, S. Haque, J. Borme, H. Aguas and E. Fortunato, *Adv. Mater. Interfaces*, 2018, **5**, 1701101.
29 K. Gao, Q. Bi, X. Wang, W. Liu, C. Xing, K. Li, D. Xu, Z. Su, C. Zhang and J. Yu, *Adv. Mater.*, 2022, **34**, 2200344.
30 S. M. George, *Chem. Rev.*, 2010, **110**, 111–131.
31 R. L. Puurunen, *J. Appl. Phys.*, 2005, **97**, 121301.
32 M. Knez, K. Nielsch and L. Niinistö, *Adv. Mater.*, 2007, **19**, 3425–3438.
33 C. Altinkaya, E. Aydin, E. Ugur, F. H. Isikgor, A. S. Subbiah, M. De Bastiani, J. Liu, A. Babayigit, T. G. Allen and F. Laquai, *Adv. Mater.*, 2021, **33**, 2005504.
34 S. Lan, W. Zheng, S. Yoon, H. U. Hwang, J. W. Kim, D.-W. Kang, J.-W. Lee and H.-K. Kim, *ACS Appl. Energy Mater.*, 2022, **5**, 14901–14912.
35 Y. Zhou, Y. Li, J. Luo, D. Li, X. Liu, C. Chen, H. Song, J. Ma, D.-J. Xue and B. Yang, *Appl. Phys. Lett.*, 2017, **111**, 013901.
36 C. Wang, S. Lu, S. Li, S. Wang, X. Lin, J. Zhang, R. Kondrotas, K. Li, C. Chen and J. Tang, *Nano Energy*, 2020, **71**, 104577.
37 G. Li, Z. Li, X. Liang, C. Guo, K. Shen and Y. Mai, *ACS Appl. Mater. Interfaces*, 2018, **11**, 828–834.
38 K. Shen, C. Ou, T. Huang, H. Zhu, J. Li, Z. Li and Y. Mai, *Sol. Energy Mater. Sol. Cells*, 2018, **186**, 58–65.
39 K. Yang, B. Li and G. Zeng, *Sol. Energy Mater. Sol. Cells*, 2020, **208**, 110381.
40 D. Ren, B. Fu, J. Xiong, Y. Wang, B. Zhu, S. Chen, Z. Li, H. Ma, X. Zhang and D. Pan, *Adv. Mater.*, 2025, **37**, 2416885.
41 C. Chen, W. Li, Y. Zhou, C. Chen, M. Luo, X. Liu, K. Zeng, B. Yang, C. Zhang and J. Han, *Appl. Phys. Lett.*, 2015, **107**, 043905.

42 E. Cho, S.-J. Sung, K.-J. Yang, J. Lee, V.-Q. Hoang, B. Kadiri-English, D.-K. Hwang, J.-K. Kang and D.-H. Kim, *J. Mater. Chem. A*, 2025, **13**, 8507–8517.
43 S. Dias, B. Murali and S. Krupanidhi, *Sol. Energy Mater. Sol. Cells*, 2015, **143**, 152–158.
44 Q. Xie, Z. Liu, M. Shao, L. Kong, W. Yu and Y. Qian, *J. Cryst. Growth*, 2003, **252**, 570–574.
45 T. Zhai, M. Ye, L. Li, X. Fang, M. Liao, Y. Li, Y. Koide, Y. Bando and D. Golberg, *Adv. Mater.*, 2010, **22**, 4530–4533.
46 Z. Cai, B. Che, Y. Gu, P. Xiao, L. Wu, W. Liang, C. Zhu and T. Chen, *Adv. Mater.*, 2024, **36**, 2404826.
47 S. K. Kim, H. K. You, K. R. Yun, J. H. Kim and T. Y. Seong, *Adv. Opt. Mater.*, 2023, **11**, 2202625.
48 N. Ahmad, Y. Zhao, F. Ye, J. Zhao, S. Chen, Z. Zheng, P. Fan, C. Yan, Y. Li and Z. Su, *Adv. Sci.*, 2023, **10**, 2302869.
49 W. Yang, J. H. Kim, O. S. Hutter, L. J. Phillips, J. Tan, J. Park, H. Lee, J. D. Major, J. S. Lee and J. Moon, *Nat. Commun.*, 2020, **11**, 861.
50 Y. M. Lee, B. K. Jung, J. Ahn, T. Park, C. Shin, T. N. Ng, I. S. Kim, J. H. Choi and S. J. Oh, *Adv. Electron. Mater.*, 2022, **8**, 2200297.
51 A. Chen and K. Zhu, *Sol. Energy*, 2014, **107**, 195–201.
52 C. Otalora, M. Botero and G. Ordonez, *J. Mater. Sci.*, 2021, **56**, 15538–15571.
53 N. Maticiuc, A. Katerski, M. Danilson, M. Krunks and J. Hiie, *Sol. Energy Mater. Sol. Cells*, 2017, **160**, 211–216.
54 R. Ortega-Borges and D. Lincot, *J. Electrochem. Soc.*, 1993, **140**, 3464.
55 L. Protesescu, M. Nachtegaal, O. Voznyy, O. Borovinskaya, A. J. Rossini, L. Emsley, C. Copéret, D. Günther, E. H. Sargent and M. V. Kovalenko, *J. Am. Chem. Soc.*, 2015, **137**, 1862–1874.
56 T. P. Weiss, S. Nishiwaki, B. Bissig, R. Carron, E. Avancini, J. Löckinger, S. Buecheler and A. N. Tiwari, *Adv. Mater. Interfaces*, 2018, **5**, 1701007.
57 S. Kim, J. Lee, D.-H. Son, W. H. Kim, S.-J. Sung, D.-K. Hwang, T. E. Hong, N. Otgontamir, E. Enkhbayar and T.-H. Lee, *Energy Environ. Sci.*, 2024, **17**, 8609–8620.
58 T. K. Todorov, J. Tang, S. Bag, O. Gunawan, T. Gokmen, Y. Zhu and D. B. Mitzi, *Adv. Energy Mater.*, 2013, **3**, 34–38.
59 K. Zeng, D.-J. Xue and J. Tang, *Semicond. Sci. Technol.*, 2016, **31**, 063001.
60 D. Lee, J. Y. Cho and J. Heo, *Sol. Energy*, 2018, **173**, 1073–1079.
61 A. K. Jain, R. Anandan and P. Malar, *Mater. Res. Express*, 2023, **10**, 105502.
62 V. Kumar, E. Artegiani, A. Kumar, G. Mariotto, F. Piccinelli and A. Romeo, *Sol. Energy*, 2019, **193**, 452–457.
63 M. Leng, M. Luo, C. Chen, S. Qin, J. Chen, J. Zhong and J. Tang, *Appl. Phys. Lett.*, 2014, **105**, 083905.
64 L. Huang, J. Yang, Y. Xia, P. Xiao, H. Cai, A. Liu, Y. Wang, X. Liu, R. Tang and C. Zhu, *J. Mater. Chem. A*, 2023, **11**, 16963–16972.
65 S. Yao, J. Wang, J. Cheng, L. Fu, F. Xie, Y. Zhang and L. Li, *ACS Appl. Mater. Interfaces*, 2020, **12**, 24112–24124.